Ice ridge density signatures in high resolution SAR images

Mikko Lensu and Markku Similä

Finnish Meteorological Institute(FMI), Marine Research, Erik Palménin aukio 1, 00560 Helsinki, Finland

Correspondence: Mikko Lensu (mikko.lensu@fmi.fi)

Abstract. The statistics of ice-ridging signatures were studied using high (1.25 m) and medium (20 m) resolution SAR images over the Baltic sea ice cover, acquired in 2016 and 2011, respectively. Ice surface profiles measured by the 2011 airborne campaign were used as validation data. The images did not delineate well the individual ridges as linear features. This was

5 assigned to the random occurrence of such ridge rubble arrangements that generate bright SAR returns. Instead, the ridging signatures were approached in terms of the local density of bright returns selected by a variably bright pixel percentage (BPP). Density was quantified by counting bright pixel numbers (BPN) in pixel blocks with variable side length L. A statistical model for BPN distributions was determined by considering how the BPN values change with the BPP and was found to apply over a wide range of values for BPP and L. The statistical approach was also able to simulate a higher BPP image when seeded

10 by a low BPP image. It was also found to apply to surface profile data analysed by counting ridge sail numbers in profile segments of variable length L. This provided a statistical connection between the bright pixel density and the ridge density. The connection was studied for the 2011 data in terms of surface rubble coverage estimated both from the medium-resolution image and from the surface profiles. Apart from a scaling factor, both were found to follow the same distribution.

Keywords: sea ice, ice ridges, ridging parameters, Synthetic Aperture Radar (SAR), X-band, TerraSAR-X, statistical analysis,

15 simulation.

1 Introduction

The ports of the northern Baltic Sea are kept accessible by icebreakers during severe winters, and there exists a demand for accurate ice information, especially on ice ridging. Ridge fields increase collision and besetting risks and reduce the predictability of shipping operations. In the Finnish-Swedish ice charts, ridging is coded by the degree of ice ridging (DIR), which is a nu-

20 meral based on icebreaker observations and manually interpreted SAR images. Due to the qualitative nature of DIR, a need for SAR methods to retrieve quantitative ridging parameters persists. The usual surface parameters are ridge sail height and ridge density, which can be used to parameterise associated statistical models. Ridge sail height and ridge density are also related to the fraction of the surface area covered by ridge rubble, a parameter that contributes to the magnitude of σ° in SAR images. The surface statistics can be linked to the subsurface ridge keel statistics with cross-sectional models, providing an estimate of

25 the total mass of ridged ice.

SAR research has approached ridging from two main directions. Physics-based approaches seek to determine the microwave backscattering properties of ridged ice, while image-based approaches seek to retrieve ridging with image segmentation methodologies, trained and validated by field data.

It is still not well-understood how the pixel-to-pixel intensity variations relate to the variation in ridging. Backscattering from rough surfaces like brash and sastrugi may overwhelm the ridging signatures, and changes in temperature, moisture and snow cover may alter their discernibility. Air temperatures around 0 degrees reduce the penetration depth of microwaves into the snow layer, decreasing the backscattering. For high frequencies, volume backscattering may exceed surface backscattering (Albert, 2012). For low-salinity ice, the scattering is dominated by volume inhomogeneities in the uppermost layers of the ice, which in part explains the high variation of X-band $\sigma°$ values for the northern Baltic Sea ice (Dierking, 1999). As the resolution of operative SAR data is usually not better than 100 m the $\sigma°$ values come from varying assemblages of ridge rubble and other surface types. Correlations between SAR signature and ridged ice volume emerge, as shown in the Beaufort Sea study of (Melling, 1998), but quantitative estimates are hard to obtain.

In the Baltic, physical backscattering was studied extensively in the 1980s and 1990s. This included models taking the sail block angle distributions into account. According to the 3D model of (Manninen, 1992, 1996), the most important ice properties in the C-band backscattering from ridges are microscale surface roughness, dielectric constant and sail block geometry. The main difference between ridged and level ice was that backscattering from ridge blocks has a broad range of incidence angles, whereas level ice has a narrow range. On the other hand, using a 2D model describing the sail as a collection of circular facets with variable surface roughness, (Carlström and Ulander, 1995) concluded that specular reflections are dominant. Both models predict rather similar results due to the broad distributions of ridge block orientations and dimensions. Ridge backscatter has also been observed to be slightly sensitive to the radar azimuth angle by (Johansson et al., 1992).

Baltic image-based research has mostly used nonlinear regression and Bayesian methods to classify ridged ice types. (Similä et al., 1992) found reasonable results using surface profile data and tail-to-mean ratio computed from the SAR pixel value distribution as a predictor. Utilising 3D scanner data, (Similä et al., 2010) demonstrated that in dry and cold ice conditions with thin snow cover, a correspondence between freeboard and C-band SAR can be found if the dominant ice thickness is known.

In (Mäkynen and Hallikainen, 2004) the $\sigma°$, distributions were computed for several ice deformation categories and incidence angles from scatterometer campaign data. Only small differences were noticed between the X- and C-band or different polarisations with the exception of HV-polarization. This agrees with the results of (Eriksson et al., 2010). The same scatterometer data was utilised in the hierarchical Bayesian model of (Similä et al., 2001). (Gegiuc et al., 2018) assessed automated determination of DIR numerals in three stages: segmentation of a SAR image, computing a feature vector to each segment, and classifying the segments. Training data consisted of Gulf of Bothnia DIR numerals from ice charts. In addition, a clear correlation between DIR numerals and deformed ice volume was demonstrated using surface profile data.

2   Data and methods

2.1   Data

Two modes of TerraSAR-X (TSX) satellite data were used. The medium -resolution HH-polarized ScanSAR image was acquired on 28 February 2011 over the Gulf of Bothnia. The high -resolution HH-polarized Stripmap image was acquired on
5   5 March 2016 near the Hailuoto island in the Bay of Bothnia. Surface profile data was collected in the Bay of Bothnia during $2-7$ March 2011 along tracks shown in Fig. 1.

The ScanSAR swath width is 100 km and the azimuthal length ofis 150 km, while in the studies, a 106x94 km subimage was used. The image was land masked and rectified to Mercator projection with reference latitude 61°40' N and pixel size 20 m. As the incidence angle range from 29.5° to 38.7° is narrow, no incidence angle corrections were done, (Mäkynen et al., 2002),
10   only the calibration of the backscattering coefficients $\sigma°$.

The Stripmap image is a Geocoded Ellipsoid Corrected (GEC) product without any terrain correction and a Spatially Enhanced Product (SE) designed for the highest possible square ground resolution. The image was rectified into 1.25 m resolution in the Mercator projection. The covered area is about $33.6 \times 42 \text{km}^2$ (width $\times$ length), from which a $19 \times 19 \text{km}^2$ km subimage was used in the analyses.

15   The ice profile dataset comprising 2800 km of the profile was collected during the week after the ScanSAR acquisition. The helicopter-borne system was similar to that described by (Haas et al., 2009). Only the LIDAR surface profile data is used here, while the electromagnetic (EM) ice thickness has been addressed in (Ronkainen et al., 2018). The analysis of LIDAR data followed standard procedures. After a reference-level determination, the local maxima were identified by the Rayleigh criterion that demands that for two successive maxima, the minimum elevation between them must be less than half from
20   either maximum. Otherwise, the shallower one is not counted. The elevation distribution of maxima has a negative exponential tail for values higher than 0.4 m, which was selected as the cutoff elevation. Above the cutoff, the maxima are assumed to be ridge sails. The average sail height and ridge densities are 0.65 m and 11.7 1/km, respectively.

The winter prior to the ScanSAR acquisition and profiling campaign was colder than average. During the campaign, SW winds up to 18 m/s triggered opening and deformation periods in the Bay of Bothnia, and the drift speed of the research vessel
25   Aranda serving as the campaign base was typically 0.1–0.4 knots. The ice thickness varied from 30 to 60 cm in pack ice. The air temperature increased from -10 C° on 24 February to -1.5 C° on 27 February. When the ScanSAR image was acquired, T_a was -2.3 C° at the Aranda base. Snow lines measured during 2–4 March had a mean thickness of 8 cm and a standard deviation of 11 cm. About 50 cm thick snow accumulations were often found by ridges, sometimes covering shallower sails. On 3 March, the snow already had some moisture, and the density varied from 0.2 to .3 kg/m3 on level ice and 0.3-0.4 kg/m3
30   near ice ridges. It can be assumed that during the ScanSAR acquisition prior to the campaign, the snow was still dry and did not significantly affect the backscattering.

The winter of 2016 was mild, and only the Bay of Bothnia had an ice concentration of 100%. Recurrent periods of mostly SW winds induced cycles of deformation, opening and freeze-up. Only in the beginning of March did the basin attain a more persistent ice cover consisting of ridged and rafted ice types. On 5 March, the fast ice thickness in the NE quadrant of the basin

was 50–65 cm, the level of ice thickness in the ridged ice pack was 30-50 cm and the air temperature was from -1 to 4 degrees. The temperature stayed below zero, and no snowfall occurred during the 10 days before the Stripmap SAR image acquisition date when the snow thickness on the mainland was about 30 cm.
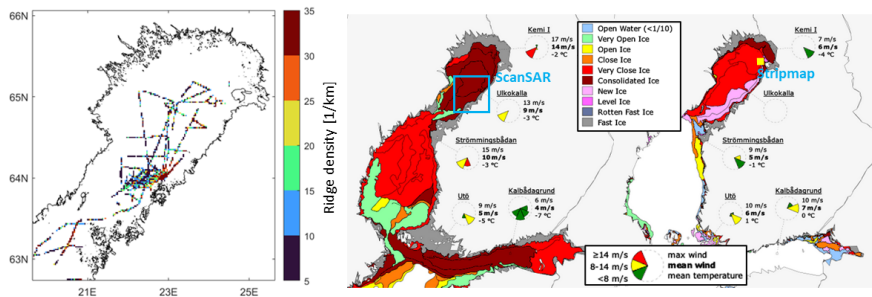
Figure 1. The profiling measurement lines during the 2011 field campaign.

2.2 Approach

5   From the backscattering viewpoint, the principal quantity to describe ridging is the relative area of ice surface covered by ridge rubble (rubble coverage). Curvilinear ridge sails are often visible, having a roughly triangular cross-section and a typical scale of 1–10 m in the across sail direction and tens to hundreds of metres in along sail direction. However, less well-defined block accumulations are also understood here as ridging as they contribute to the rubble coverage. Their signatures in surface profiles are also similar to those of curvilinear ridges.

10   It appears clear that the returns from the ridge rubble dominate the brighter end of the backscattering intensity histogram. The brightness statistics involve a certain uncertainty, however. The histogram depends on the processing of the image aimed at a good visual appearance. A change in ambient conditions may result in quite different intensity histograms for an otherwise unchanged ice cover. Still, an ice charting expert can typically recognise in both cases the same ridging signatures as these appear persistent and symptomatically nonhomogeneous. The persistence shows up clearly in binary images comprising a

15   certain percentage of bright pixels from the intensity histogram tail. If the percentage is reduced, the ridging signatures become more sparse but tend to retain structural congruence with the non-reduced signatures.

In a way, the objective of the present approach is to provide a statistical foundation for the assessment that the ridging signatures in two SAR images 'look the same'. Towards this end, a certain bright pixel percentage (BPP) is selected with an intensity threshold. For a higher BPP, the selected bright pixels are expected to be predominantly returns from ridge rubble.

20   The spatial variation related to the ridging signatures is described in terms of the bright pixel number (BPN) in pixel blocks with side length L, or equivalently in terms of the bright pixel coverage (relative area, density) in the blocks. The side length L and the BPP are variable parameters of the BPN approach.

Proper validation data for the BPN approach would consist of ridge rubble topography in square areas with a comparable side length, for example, scanning LIDAR data over snow-free ice. The extent of such data is limited, however. The validation

data, therefore, consists of linear surface profiles from which ridge sails are identified. The profiles are divided into segments of length L, and the ridge sail numbers (RSN) in the segments are counted. Only those sails are counted that exceed a certain height threshold. The ridge rubble coverage will inherit the RSN statistics that can then be parametrically compared with BPN statistics for concurrent datasets. The segment length L and the sail height threshold are variables of the RSN approach.

5   As the BPN and RSN approaches are formally analogical, a more theoretical validation exercise seeks to show that they follow the same statistical model. The model is derived by considering how BPN and RSN values change with threshold changes (threshold process). High-resolution (1.25 m) images resolving individual ridge sails are used.

2.3   Estimating ridge rubble coverage

Ridge rubble coverage can be estimated along a linear profile from ridge sail height and ridge density. To provide realistic
10   estimates, the effect of the cutoff sail height used in the profile analysis must be assessed, as well as the application of results reported on the sail $width/height$ ratio, which is noted as $R = w/h$. Considering first the ridge width, the effect of oblique angles of sail crossings must be taken into account. For randomly oriented ridges, the average width is $\pi/2$ times the perpendicular width (Mock, 1972). The reported R ratios for perpendicular width are usually around 4. However, the measurements typically refer to the highest point of some sail section, while aerial imagery shows that the sail width does not vary as much
15   as the sail height but is rather constant. The results of (Lensu, 2003) indicate that the highest point of a sail section is typically 2.5 times the average sail height, and thus the average value of R random sail crossings is about 10. To add, the Rayleigh criterion counts as singular ridges certain wider multiple peaked formations. Deformed ice fields also include scattered rubble and other diffuse roughness not accounted for in the estimates. To include the contribution of these, the value $R = 13$ is adopted.

     The cutoff sail height affects both ridge density and ridge height. To estimate the cutoff effect, the extrapolation model by
20   (Lensu, 2003) is applied. It is assumed that the average sail height is representative of the whole data set and only the variation of ridge density is at issue. For the present LIDAR profile data with a cutoff height of 0.4 m and an average sail height 0.65 m, the model provides estimates that the true average height is $h_a = 0.48$ m and that the true densities are 2.0 times the observed density.

     Taken together, the ridge rubble coverage RRC along a profile is:

$$
25 \quad \frac{RRC}{A} \quad = \quad \frac{\pi}{2} \times R \times h_a \times 2 \times \lambda \tag{1}
$$

$$
= \quad \frac{\pi}{2} \times 13 \times 0.00048 \times 2 \times \lambda, \tag{2}
$$

where all quantities are in kilometres (h_a=average height, λ=observed ridge density). A unit increase in the observed ridge density for 0.4 m cutoff data increases the along profile rubble coverage by 1.96%. However, as the interpolation factors are rough estimates, the value 2% is used instead.

30   If the profiling flights have crossed an area multiple times in different directions, which for our data was the case for coastal ridge fields near the flight base, the estimate is representative of areal rubble coverage. For a singular crossing, the relationship involves randomness and is generally the more reliable the larger the considered area is, provided that homogeneity of ridging conditions persists. On the other hand, independent estimates of rubble coverage from SAR or other data can be converted to

ridge density interpreted either as an average of multiple crossings or as the probability to find the said density in a singular random crossing.

2.4 Threshold process

For an idealised SAR image with accurate real-valued intensities, the pixel values can be arranged into strictly increasing order. Starting from an empty image matrix and from the brightest pixel, the pixels of the ordered series can then be added to the matrix one by one. It can then be studied how the probability for the BPN to increase by one depends on the pixel block state $< L, BPN, \dots >$ as defined by L, BPN, and possibly by other descriptors. The probabilities can then be used to formulate recurrence relations generating finite BPN distributions.

For integer-valued SAR images, the process starts from the BPN values for maximum intensity and proceeds in unit integer steps by adding pixels of subsequent lower intensity. This is designated as the threshold process. The increase probabilities are replaced by increase rates, that is, the relative number of events of unit BPN increase. For RSN, an analogical process decreases the sail height threshold by small values, starting from a threshold equalling the highest ridge. The increase rates of the threshold process are then interpreted as increase probabilities of an idealised process. This is legitimate if the number of increase events larger than unity is relatively small for each step.

The threshold process is continued to a certain pixel intensity or ridge sail height cutoff, called a target threshold. The derivation of the statistical model is based on the following observation. The intensity or ridge sail height values higher than or equal to the target threshold can be randomly permuted. This changes the increase rates, generating another threshold process. However, the BPN or RSN distribution observed on the target threshold level is the same for both processes. Thus, the new increase rates can be used to generate the observed distribution. The random permutation has the merit of removing the spatial correlations of intensities or sail heights so that the threshold process is reduced to a random deposition process.

2.5 Scale system of distributions

The threshold process and the distribution model are presented for RSN statistics. The case for BPN is conceptually analogical but involves complications not present in RSN statistics: discreteness of integer data, resolution set by pixel size, and L^2 as the maximum BPN value.

In RSN analysis, surface profile data is divided into segments, and the numbers n of sails in the segments are counted. A discrete distribution $k(n_i)$ for sail number n_i becomes defined for each scale L_i. If $L_j < L_i$ is a shorter segment, a conditional distribution $k(n_j|n_i)$ becomes defined. This can be interpreted as the conditional probability to find n_j sails in an L_j-segment nested inside an L_i-segment containing n_i sails. The $k(n_j|n_i)$ can be also called downscaling probabilities as they can be used to derive distribution $k(n_j)$ from $k(n_i)$. The approach can be extended to a cascade of scales, constituting a scale system of distributions.

In an ideal threshold process, the sail heights are arranged into strictly increasing order and added one by one to the segmented profile. Two nested segments with lengths $L_i > L_j$ are considered so that the longer segment L_i is divided into segments with length L_j and $L_i - L_j$. If the sail is added in the process to L_i-segment, it has a certain probability of getting

added to each subsegment. This probability must satisfy the additivity condition $P(L_i) = P(L_j) + P(L_i - L_j)$. The simplest assumption satisfying the condition is $P(L_i) \sim n_i + aL_i$, which leads to the hypergeometric distribution (Lensu, 2003):

$$k(n_j|n_i) = \frac{\binom{aL_j+n_j-1}{n_j}\binom{aL_i-aL_j-1+n_i-nj}{n_i-n_j}}{\binom{aL_i+n_i-1}{n_i}}, \quad n_j = 0, 1, \ldots, n_i. \tag{3}$$

If $L_i/L_j \gg 1$, then the finite and discrete distribution $k(n_j|n_i)$ is approximated by $k(n_j)$ and $k(n_j)$ is approximated by the negative binomial distribution

$$k(n_j) = \binom{aL_j + n_j - 1}{n_j} p^{aL_j}(1-p)^{n_j}, \quad \text{where} \quad p = \frac{aL_j}{aL_j + <n_j>}, \tag{4}$$

and furthermore, if $<n_j>$ is large, the continuous approximation of Eq. 4 is the gamma distribution:

$$f(n_j) = \frac{1}{\Gamma(\alpha)}\beta^{\alpha}n^{\alpha-1}e^{-\beta n_j}, \quad \alpha = aL_j, \quad \beta = \frac{aL_j}{<n_j>}. \tag{5}$$

It is convenient to assume that L_i is a regional scale where ridging statistics are described by the negative binomial $k(n_i)$, as approximated by the gamma distribution. The hypergeometric $k(n_j|n_i)$ is then be used to describe local variation.

The statistical model is validated in two stages. First, the additivity condition is validated by conducting a threshold process for selected scales and target thresholds and observing whether the increase rates have a linear dependence on the RSN or BPN. In the next stage, the distribution models are fitted to the data. In the sections to follow, this is done by the observed mean and variance, and the goodness of fit is checked. The parameter a is obtained from the variance

$$var(n_j|n_i) = \frac{L_j n_i(aL_i + n_i)(L_i - L_j)}{L_i^2(aL_i+1)} \tag{6}$$

and

$$var(n_j) = \langle n_j \rangle + \frac{\langle n_i \rangle^2}{aL_j} \tag{7}$$

for the hypergeometric and negative binomial models, respectively. The variance for the negative binomial distribution is larger than the mean, which ensures that a is positive in Eq. 7. The parameter a quantifies the relative strength of the component process of the random spatial deposition of sails, that is, the Poisson process. If the validation results agree for test cases selected from a certain scale range, it can be concluded that the scale system is applicable over the scale range.

2.6 Simulation of SAR texture by the threshold process

To analyse the BPN threshold process in full detail requires that bright pixels are added one by one in process steps. For integer-valued images, this cannot be attained. On the other hand, it is possible in a validation approach where the generative hypotheses are tested by simulating the generative process. The simulation commences from a certain stage of the observed threshold process. New bright pixels are added one by one following the assumed probabilities and possibly other conditions. The simulated result is then compared with the observed one.

A binary image with value 1 (white) for an observed low percentage of brightest pixels is used to seed the process. The simulation changes the value of black (zero) pixels into white, one at a time. This is done by a scale cascade, which is assumed here to follow the linear generative hypothesis. The first step divides the image into four rectangles along randomly chosen vertical and horizontal lines. To each rectangle is assigned weight $aN0 + N1$, where $N0$ is the number of pixels, $N1$ is the number of white pixels, and $a < 1$ is a parameter that controls the relative strength of a random spatial placement (Poisson process). One of the rectangles is selected for the next step with a probability defined as the ratio of rectangle weight to the sum of weights. The selected rectangle is divided further into four, and the cascade is continued until the rectangle contains only one black pixel that is changed to a white pixel. The process repeats until a preset number of white pixels is reached.

The simulation approach can also be applied to other generative hypotheses. Imposed maps of spatially distributed weights can be used to include spatial aspects of the generative process, like correlations, homogeneity, gradients and support, i.e. the subregion outside of which the process is not active.

3 Results

3.1 Observed threshold process rates and distributions for ridge sail number

From the profile data set described in Section 2.1, profiles exceeding 5 km in length were selected and truncated to be divisible into 1.6 km, in total 2256 km. For RSN analysis the segment length L the cascade [50,100,200,400,800] (meters) was used. The threshold process decreased in 0.01 m steps from 2.5 meters (10 ridges). The target threshold was set to 0.5 m (18638 ridges).

The increase rates per step were determined as the mean value of RSN increases, including zero increase, and the presented results are for the pooled data comprising all steps to the 0.5 m target threshold. The increase rates were calculated both for the original data and for randomly permuted sail heights. The results shown in Fig. 2 disregarded the tail part with an excessive variation. In the right panel of Fig. 2, the highest RSN values correspond to ridge density 160/km, a value characteristic of rubble fields with no level ice visible. The increase rates were linear with a slight superlinear bend.

The rates for non-randomised data deviate after beginning from linear to sublinear increase. For other scales, the behaviour was similar, and for long L, the rate more or less settled to a constant value in its tail part. A likely reason is that sail height correlations that arise naturally as block thickness (a parameter controlling ridge sail height) vary spatially during the course of the ice season. Correlations were indeed found between RSN and the average sail height.

The hypergeometric and negative binomial distributions were fitted to the data with observed mean and variance. The negative binomial $k(n_i)$ agrees well with the empirical distributions derived from the full dataset in Fig. 3. Only the number of empty segments is overestimated for 200 m and 400 m segment lengths. Fig. 4 shows the hypergeometric distributions $k(n_j|n_i)$ for the conditioning scale $L_i = 1600$ m and for the range [50,100,200,400] of the subsegment scale L_j. The results for two values of conditioning RSN, $n_i = 16$ and $n_i = 72$, are shown. These are equivalent to ridge densities 10/km and 45/km for the segments L_i. The agreement is good, considering that the subset size is limited by fixed value n_i. Similar results are found for other combinations of L_i, L_j, and n_i.

The hypergeometric model was derived from the assumption that the rate of the RSN increase for the segment length is proportional to $n + aL$. The parameter a is obtained from the mean and variance and is generally found to decrease with L following the power law. For the hypergeometric case shown, the exponent has about the same value of 0.5 for all values of the conditioning n_i from 16 to 72. The parameter a was interpreted as the relative Poisson intensity, which also provides the rate of sail appearances to empty segments in the threshold process. If there is no rubble present in the segment, it can be said to consist of level ice and cannot experience a change of RSN from 0 to 1, either. The Poisson parameter of level ice segments is zero, and the observed Poisson parameter a is obtained by multiplying the true Poisson parameter of rubble segments by their relative coverage. Thus the power law suggests that the area covered by ridge rubble has fractal geometry.
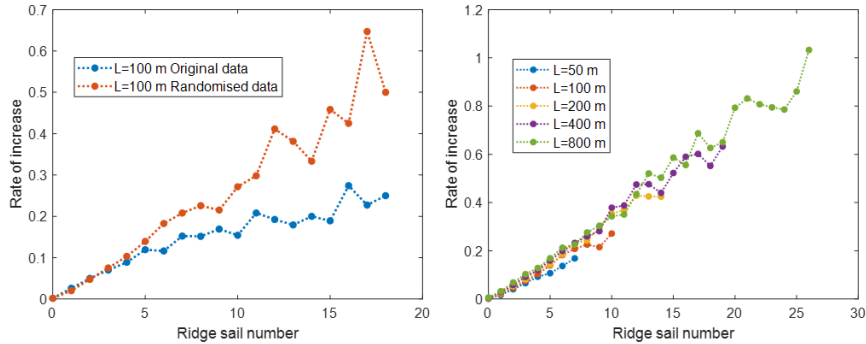
Figure 2. Sail number increase rate for a threshold process with target threshold 0.5 m. Left: Rate for observed sail heights and randomised sail heights for segment length $L = 100$ m . Right: Rates for randomised sail heights for different segment lengths.
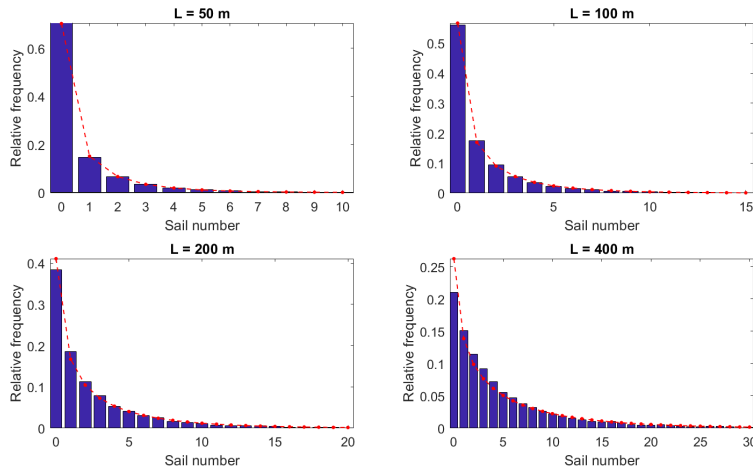
Figure 3. Negative binomial fits to the RSN distribution for the full LIDAR dataset and for different segment lengths.
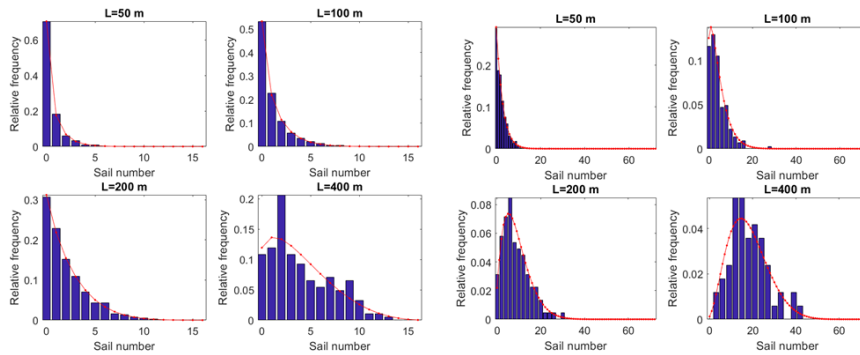
Figure 4. Hypergeometric fits for distributions $k(n_j|n_i)$ conditioned by $L_i = 1600$ m and $n_i = 16$ (left panel group) and $n_i = 72$ (right panel group). The scales L_i belong to [50,100,200,400].

3.2 Characteristics of high-resolution SAR

The pixel size of the March 2016 Stripmap image is 1.25 m, which resolves backscattering signatures from individual ridges. The size of the image (Fig. 5) is 19x19 km, but for analysis and visualisation, different subimages were also used, principally 7000x7000 (8.7x8.7 km) and 1024x1024 (1.3x1.3 km)subimages with representative ridging signatures. To proceed following the approach outlined in Section 2.2, a certain bright pixel percentage (BPP) is selected and a binary image with unit values for the bright pixels is generated. The variation of bright pixel density is described in terms of bright pixel numbers (BPN) in pixel blocks with variable side length L.

Two derivative image types are also presented. Following the BPN approach, the first derivative replaces (as a sliding operation) pixel values with BPN values calculated for pixel blocks centred at the target pixel. This is accomplished by a convolution with a LxL all-ones kernel. The result is termed 'contextual image', as the visibility of ridging signatures and their effective resolution depend on BPP and block side length L, which can be chosen to suit the application context. The other derivative is 'category image', which divides the brightest 30% of pixels into three 10% classes, either for the original or the contextual image.

In the category-image version of the Stripmap image, Fig. 5, ridging features appear to be visually delineated by the brightest 20%, while the interval 70–80% begins to add more scattered pixels. The hope of a similar quasi-photorealistic appearance as is found in comparable TerraSAR-X terrestrial images by Dumitru and Datcu (2013) does not quite materialise. There are obvious linear ridges, but these consist of chains of detached bright components that do not connect to continuous features. Larger features, reminiscent of ridge groups or small rubble fields, are more readily observed. However, they are also aggregates of detached bright components, and a similar texture is also found for ship ice channels that are flat and rather uniform beds of bright scatterers. Increasing the bright pixel percentage from 30% slightly improves the connectedness of ridge signatures but at the same time obscures their delineation by adding scattered bright pixels to apparent level ice areas.
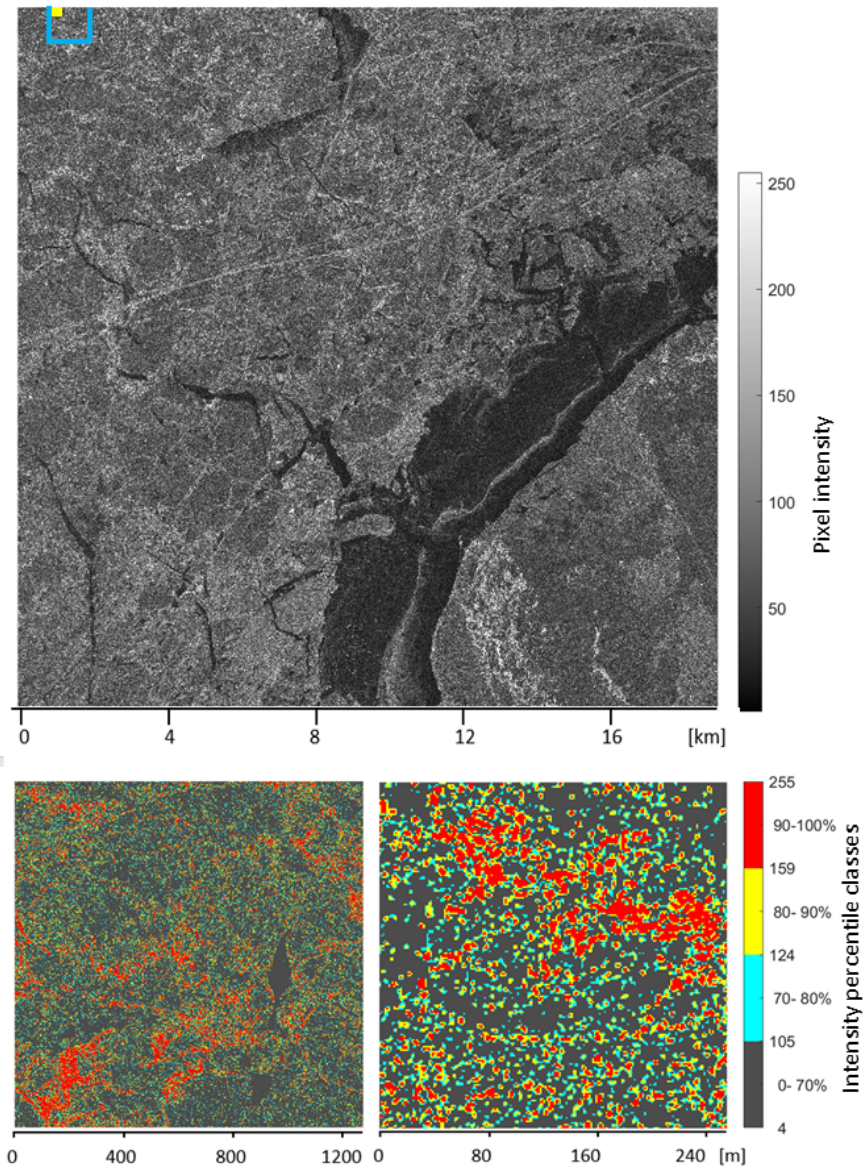
Figure 5. The 15200x15200 Stripmap image with the locations of 1024x1024 and 200x200 subimages indicated (upper panel). The 1024x1024 and 200x200 subimages (lower panel).

These observations agree with the results by (Manninen, 1992) and (Carlström and Ulander, 1995) that indicate that bright returns from ridge rubble depend on random factors like a favourable orientation of blocks, while the returns from the remaining

sail may fail to be clearly distinct from the surrounding level ice. The apparent randomness also corroborates the assumption that the density of the bright pixels in the image is proportional to the coverage of ridge rubble.

In the contextual image and its category image rendering, Fig. 6, the sliding block side length is $L = 101$ (126 m), and the BPP is chosen to be 20% or comprising the red and yellow pixels of Fig. 5. It is seen that the ridging signatures are enhanced and their connectedness improved in the contextual images.
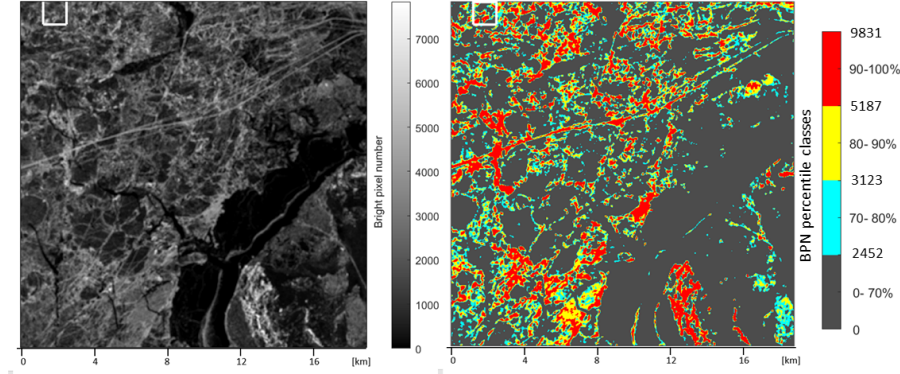
Figure 6. The 15200x15200 contextual image (on the left) and corresponding category image derived from the full image with BPP 20% and L=101.

3.3 Observed threshold process rates and distributions for high-resolution BPN

For the analyses of the 7000×7000 upper left corner subimage of the Stripmap image was used in order to avoid the refrozen lead visible in Fig. 5. The image was divided into non-overlapping pixel blocks with side length L, measured in pixels. The intensity threshold was decreased by unit integer steps, starting from 255, and the rate of BPN increase as a function of BPN was obtained for each step. In the presented results, the rate data comprises all steps down to the target threshold. In the subimage, 1.2% of the highest intensities are saturated to 255. This percentage is equal to that for the intensity band [218,254] and would correspond to the extending of the exponential tail of the intensity histogram beyond 255 to 350. This somewhat affects the results for the initial steps of the process.

Analogically to the RSN analysis, the pixel intensities above and including the target threshold were randomly permuted. In Fig. 7, the block side length is set to $L = 36$ and the target intensity threshold values [182,149,118,86] are chosen, corresponding to BPP values [5,10,20,40]. As for the RSN, the magnitude of the rates is not relevant, and they have been scaled so that the sum rate equals L^2 or 1024. The different degrees of saturation then separate the point clouds in the figure. Linearity is observed unless the saturation of the pixel block is felt after 3/4 of the block capacity is filled.

In the other test case in Fig. 8, the BPP is set to 20% (target intensity threshold 118), and the block side length increases from 4 to 128. In addition to the same scaling of rates as in the first test case, the BPN range $[0, L^2]$ has been scaled to [0,1]. The results are similar to the first test case. For comparison, the same result is shown for the original data where the pixel intensities

are not randomised. For higher L, the relationship is then approximately linear for small relative BPN values, but otherwise, it is quadratic. Intensity correlations are the likely reason, but no further conclusions are attempted.

The agreement of the proposed distribution system with the data is again good. Distributions were calculated from block tiling of the 9216×9216 (11.5×11.5 km) upper left corner subimage. Fig. 9 shows negative binomial distributions $k(n)$ fitted by observed mean and variance for BPP 10%, and three scales are shown. The fourth subplot shows the model parameter a as obtained from the mean and variance for the binary cascade of scales $L = 8,\ 16, \ldots, 256$ and for three BPP values. The power law exponents vary from -0.45 to -0.37 and are thus close to but somewhat smaller than the values obtained in the RSN analysis. Also, the negative hypergeometric model $k(n_j|n_i)$ conditioned by scale L_i and BPN value n_i applies well. Fig. 9 shows the results for selected combinations of Li, Lj and n_i. The conditioning scale cannot much exceed the value $L_i = 16$ as the number of instances n_j for conditioning pairs (L_i, n_i) decreases as L^{-4}.
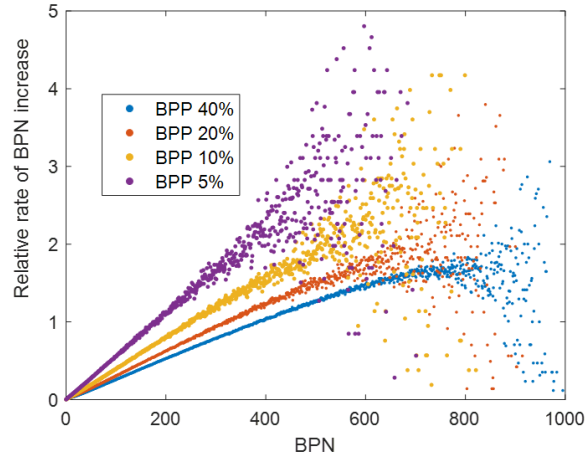
Figure 7. The BPN increase rates for pixel block side length 36 and BPP increasing from 5% to 40% in binary fashion.

3.4 Simulated high-resolution SAR texture

The simulation algorithm was applied to the 1024x1024 subimage indicated in Fig. 5. The white pixels of the initial binary image correspond to BPP 3%. The simulation added 10% so that the resulting BPP is 13%. If $aN0 \gg N1$, the Poisson process dominates the simulation step, but overall, the process gravitates towards image areas with a higher density of white pixels. However, if the fraction of white pixels is initially low, the Poisson component process tends to add nonzero pixels into larger empty areas, first creating dispersion and then spurious clusters. To reduce this, an additional condition requires that in a process step, a white pixel cannot be added within a rectangle if its fraction of nonzero pixels is below a threshold Co and the rectangle area measured as pixel number is within certain limits $[N1, N2]$. This effectively means restricting the support of the process.
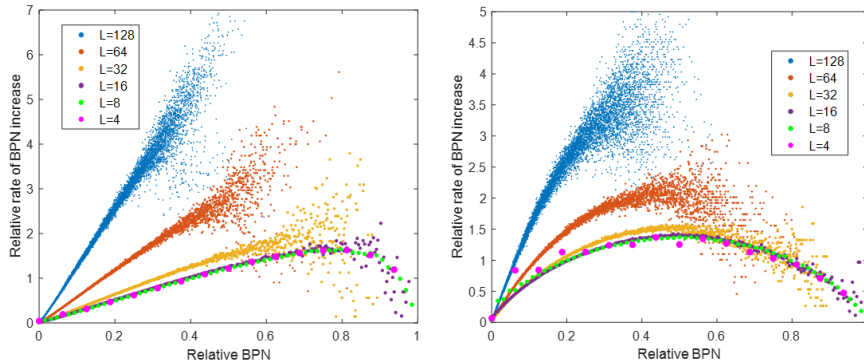
Figure 8. The BPN increase rates for BPP 20% and the pixel block side length increasing from 4 to 128 in binary fashion.
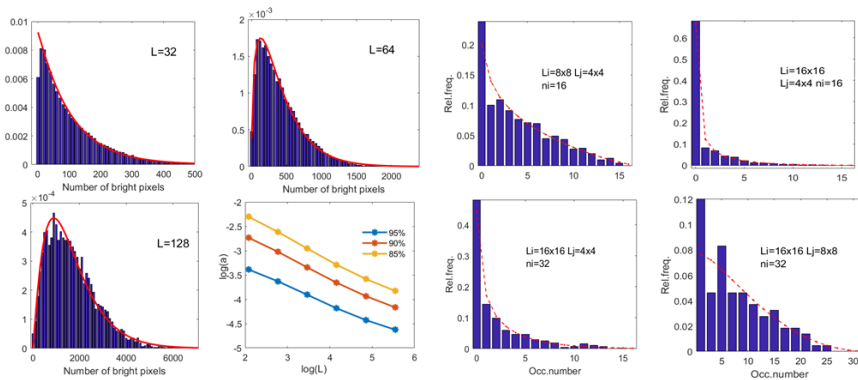
Figure 9. In the left panel group BPN distributions and their negative binomial fits for BPP 10% and three different pixel block side lengths L. The parameter a is also shown for a scale cascade $8, 16, \ldots, 256$ and for three different BPP. In the right panel group hypergeometric fits for conditional BPN distributions for different combinations of conditioning scale L_i and conditioning BPN n_i.

The parameters were $a = 1/20$, $Co = 1/100$ and $[N1, N2] = [100, 20000]$, and the results are shown in Fig. 10. Although not matching exactly on the pixel level, both 13% images exhibit the same pixel density variations. For contextual and category images for $L = 21$, the results for the real and simulated 13% images match almost exactly, that is, they contain the same information at scale $L = 21$. The results provide additional corroboration for the soundness of the generative hypothesis. They also provide the insight that certain parts of 'non-deformed' ice should be left outside the ridging statistics, a feature also previously suggested by the emergence of power law exponents for the parameter a in the distribution fits. The parameters of this demonstration were determined by simple experimentation, but more systematic approaches can be conceived. Especially, intensity values could be incorporated, which would introduce spatial intensity correlations, and the fractality suggested by the distribution analysis could be encoded into the simulation steps.
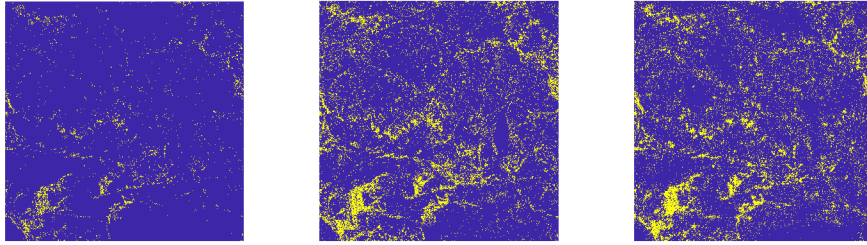
Figure 10. BPP 3% binary image, BPP 13% image, and the BPP 13% image generated from the BPP3% image by the simulation algorithm.

3.5 SAR and LIDAR comparison for the 2011 image

The analysis of ridged areas in the 20 m resolution TSX ScanSAR image proceeds in a similar manner as the analysis of high-resolution SAR data. The basic SAR tools are the bright pixel percentage (BPP) and the counting of bright pixel numbers (BPN) in pixel blocks. The target is distributions $f(x)$, where x is the estimated ridge rubble coverage (RRC) in pixel blocks

5 (SAR RRC) or their ground truth counterparts as determined from LIDAR surface profiling flights (LIDAR RRC).

The essential assumptions are that LIDAR RRC can be estimated from profile data, Section 2.3, that the bright pixel number can be used as a proxy for SAR RRC and also for 20 m resolution data, and that both RRC concepts inherit their statistics from the model for RSN and high-resolution SAR BPN, sections 3.1 and 3.3. It is noted that the 20 m resolution can still detect much of the ridging signature in Fig. 11 and that the simulation method described in Section 2.6 works.

10 The BPP is set to 20%. The exact BPP value is not essential, but the chosen one is expected to comprise most of the ridging signatures and not too much level ice. Similarly, as for the high-resolution image, the bright pixels are mostly not connected to continuous ridging features. A convolution operation is then conducted, generating a contextual image Fig. 11, where each pixel value of the original image is replaced by the number of bright pixels (BPN) in a 15 by 15 pixel block centred at the pixel. As the target is rubble coverage, the BPN values are changed to percentage points. The convolution operation acts similarly as

15 in the high-resolution SAR and effectively reveals the ridged areas and connects many of the ridging structures that are only vaguely discernible in the original SAR imagery.

For comparisons between the SAR RRC and LIDAR RRC, the resolution of the contextual image is weakened to 1 km^2. This coarser scale image Fig. 12 is called an analysis image, and its pixel value is the mean of all pixels inside the corresponding contextual image pixel block. These pixels represent the SAR RRC and are compared with LIDAR RRC values determined in

20 grid cells matching the pixels with respect to size and location. The LIDAR data were assigned to the grid cells in Fig. 12 using the coordinates included in the data. If the LIDAR grid cell contains data, its value is the ridge density detected in it, and the RRC in percentage points is estimated by multiplying the density by 2%, Eq. 5. Ridge densities larger or equal than 50 then have 100% RRC. This was the case for about 2% of all the cells with nonzero ridge density and occurred only in the rubble field zone close to the eastern coast.

As mentioned in Section 2.1, ice drift and deformation occurred during the profiling campaign week after the acquisition of the SAR image. As the ice drift could have been well over 10 km during the time gap, and the flights are from several days, it is not possible to establish a pairing between the two RRC estimates in SAR analysis pixels and LIDAR grid cells, and the comparison was made regionally. All LIDAR data in the area covered by the SAR image was used for the RRC values in the LIDAR grid, Fig. 12. The SAR RRC analysis image Fig. 12 includes all pixels outside the mask (N=7549 pixels). LIDAR data (N=1017 cells) comprise about 13% of the SAR pixels.

The two datasets are compared in terms of a quantile-quantile (Q-Q) plot for the respective distributions. This can be viewed as a nonparametric approach to comparing their underlying distributions. There is also no need to compare the grid values pairwise or have equally sized datasets. The quantile pairs are largely located along a line with a ratio of 1.34 between the quantiles (Fig. 13, the left panel). This indicates that the shapes of the distributions are similar and that they may belong to the same distribution family. As LIDAR RRC is expected to follow a gamma distribution (Eq. 5), this is then also expected for SAR RCC. For two gamma distributions, the linearity of the Q-Q plot entails that the shape parameters are equal, which also holds for the model Eq. 5 if the scale L_j and the process parameter a are the same for both. The slope of the Q-Q plot then equals the ratio of the scale parameters, suggesting that a value of 1.34 can be used as a scaling coefficient.

It was examined how close to each other the distributions of the SAR and LIDAR RRC are with and without the scaling coefficient of 1.34, Fig. 13. The original SAR and LIDAR RRC densities show the same basic shape but do not match well. When SAR RRC is scaled by 1.34, the match is improved, and the obtained mean values are very close to each other: 26.2% for the scaled SAR RRC and 25.9% for the LIDAR RRC. Converting the mean values to the number of ridges yields about 13 ridges per km^2 for both data sets. Gamma distributions were also fitted to both data sets. The maximum likelihood estimates for the shape parameter of the scaled SAR RRC gamma density is 1.7 and the scale parameter 15.5. The respective values for LIDAR data are 1.4 and 18.2. Thus, although the parameters of the fits are close to each other, they are not equal.

The problems with the fit and agreement with gamma distribution mostly concern the tail part of the distribution. The linearity of the Q-Q plot was no longer valid for SAR RRC over 50 % and for LIDAR RRC over 75 % RRC. The SAR RRC values over 50% are relatively rare in the data, and highly ridged areas form proportionally a much larger fraction in the LIDAR data. Especially the rubble field hump seen by the end of the LIDAR distribution is not present in the SAR distribution. As the LIDAR flights frequently flew over the large coastal rubble field zone (see Fig. 11), a larger proportion of the LIDAR data was collected from this area than was the case with the SAR RRC data. The scaling coefficient was found to increase with the area of SAR included in the comparison and varied from 1.3 to 1.6. With a spatially more uniform coverage of the LIDAR flights over the SAR image, the agreement would probably have been better for the tail part.

As expected, decreasing the BPP value increases the scaling coefficient when the SAR image extent and the LIDAR data stay fixed. Three cases were examined: For BPP 10 %, the scaling is 2.22, for 15 %, it is 1.61 and in the above analysis with BPP 20 %, it is 1.34. In all three cases, the QQ plot is linear for its main part and the mean of the scaled SAR RRC distribution are always close to the LIDAR RRC mean.
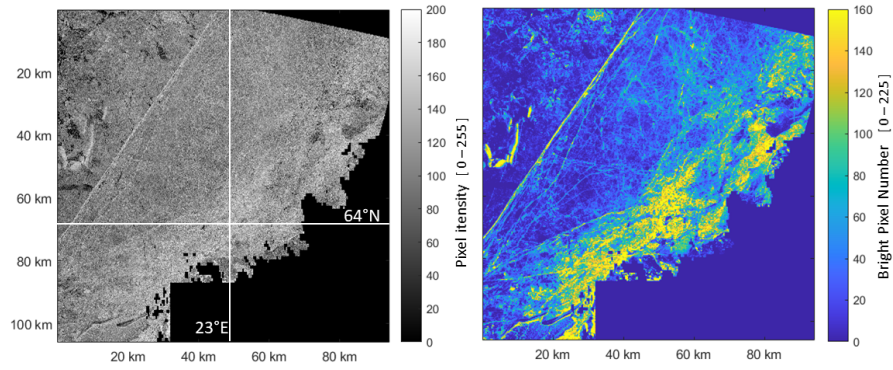
Figure 11. The test area covered by the TSX SAR imagery with resolution of 20 m. On the right is the contextual image with BPP 80%.
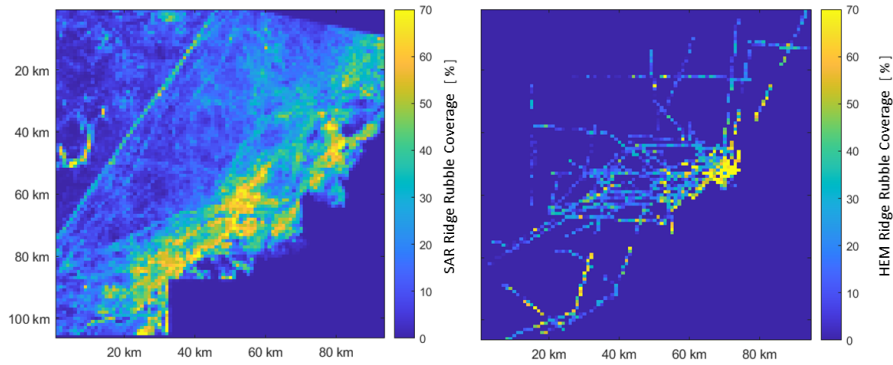
Figure 12. The analysis image over the test area presented as a SAR RRC image on the right and the corresponding LIDAR RRC image. The units are percentage points in both images.
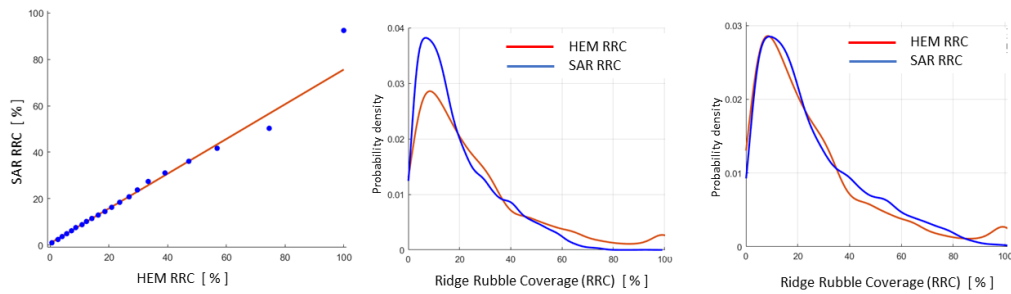
Figure 13. The quantile-quantile plot for the SAR and LIDAR data sets (left). The SAR and LIDAR RRC distributions overlaid (middle). The scaled SAR and original LIDAR RRC distributions (right).

3.6 Contextual images as ridging information

Although in SAR images from a ridged ice cover the bright returns are predominantly from ridge rubble, the step to quantitative methods has proved hard. The bright pixels do not typically connect well to ridging features. This was found here also for high-resolution SAR and was assigned to the random occurrence of favourable rubble block arrangements.

5   The randomness problem can partly be bypassed by the BPN approach as the ratios of BPN values do not change much even in large changes in BPP. Thus, the appearance of contextual images that enhance the ridging signature by a BPN sliding operation (Fig. 6 or Fig. 11) also does not change much. This appears more strikingly in the category versions of the contextual images (Fig. 6), which provide an application-oriented way to delineate ridged ice.

The upper panels in Fig. 14 show the 1024x1024 subimage of the high-resolution SAR indicated in Fig. 5 and its BPP

10   20%, $L = 21$ contextual derivative presented as a category image in the upper right panel. However, for the BPP range from 2% (pixels with value 255) to 95%, the category image is almost identical to that in the upper right panel. The same result is found for several alternative methods to generate a contextual image, like the $L = 21$ sliding block average of intensity. More strikingly, the information of the contextual image is essentially retained in different randomising transformations. In the lower left panel of Fig. 14 the 1024x1024 image has been multiplied eight times by a random matrix that erodes the ridging

15   signature almost beyond visual recognition. However, the contextual category image still emerges essentially unchanged in its main features in the right panel.

The observed behaviour is due to the fact that changes in BPP, changes in method, or randomising operations on the average preserve the order of values in the contextual images. This feature is enhanced in the category versions as the flux of values across category boundaries is then relatively small. This can be studied in detail by pixel-to-pixel mapping between two

20   contextual images. For example, mapping for the 1024x1024 subimage with $L = 21$ and BPP 20% the BPN values to matching $L = 21$ sliding intensity averages the relationship is monotonous on the average. For each BPN value, the mapped intensity averages have a normal distribution with a standard deviation in the range of 3.5–4.5. On the other hand, the widths of the $70\% - 80\%, 80\% - 90\%$ and $90\% - 100\%$ categories for the intensity average are 9, 15 and 102, respectively. Thus, the highest class, in particular, retains its delineation in this method change. More importantly, if the change in BPN values induced by

25   a change in ambient conditions preserves the order on the average, the category images can be consistently used in the daily production of ice information.

The pixel block side length L affects the resolution of detail in the contextual images, and its value may be chosen to suit the context, hence the term. Including a pragmatic viewpoint, $L = 21$ of Fig. 14 and $L = 101$ of Fig. 6 correspond to the width and length scales of icebreaking ships so that the BPN values of contextual images provide the number of bright

30   scatterers that the ship bow or the whole ship interacts with at a time. As BPN has been shown to be a proxy of ridge rubble coverage, the contextual images have direct pertinence to navigability. The categorised versions can be interpreted as classes of navigational difficulty, or as delineation of areas that a ship should not enter. They can be used in tactical navigation or in route optimisation that only seeks to avoid difficult ice types. More advanced route optimisation is based on physical models for the added resistance from the ridges. The ice-going speed and the probability of besetting can then be obtained in simulations that

take the ice conditions along alternative tracks as input, specifically ridge density and ridge height (Kuuliala et al., 2016). As the contextual images provide only relative ridge density estimates, the scaling to true values, as well as ridge height, must be determined by other means. These may include observations from ships, measurements, or satellite data, especially ICESat-2 profiles. Another possibility is to use a ship's response, observed remotely from AIS data, to classify the contextual image signatures directly in terms of ice cover resistance (Similä and Lensu, 2018).
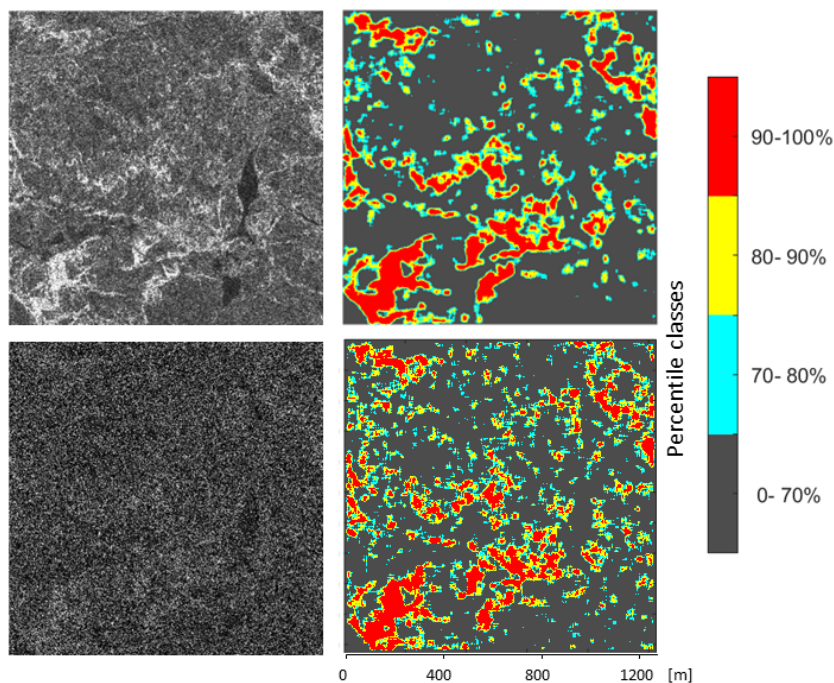
Figure 14. Results for 1024x1024 Stripmap subimage multiplied by 8 times by a random matrix. Left column: The subimage (upper left) and the randomised subimage (lower left). Right colum: Category versions of contextual images obtained by BPP 20% and 21x21 convolution kernel for the original subimage (upper right) and for the randomised subimage (lower right).

4 Discussion and conclusions

Ice charting experts are usually able to recognise the same ridging signatures in SAR images that have different resolutions or are taken in different ambient conditions. The present approach proceeded from this observation by analysing SAR images in terms of the local density of bright pixels chosen by a certain percentage (BPP). The tail intensity variations, which are often relied on in SAR ice type classification approaches, were left to a secondary role. The quantification is in terms of bright pixel numbers (BPN) counted in pixel blocks. First, high-resolution images were investigated for which the bright returns can be assumed to come from individual ridge sails. A distribution model was derived and found to apply also to ridge sail numbers

(RSN) determined for surface profile segments. A validation study using a medium-resolution SAR image with near concurrent ground truth data demonstrated that the method can be used to derive ridge density up to the scaling factor. This can be provided by independent observations, most promisingly by ICESat-2 surface profiles.

The distribution model was derived with a threshold process where bright pixels or ridge sail were deposited sequentially to the image canvas or surface profile. The probability for the deposition to end in a certain pixel block or profile segment was proportional to the corresponding BPN or RSN value. This raises the question of the role of the physical ridge formation events that manifest as the formation of new sails to profile segments or as the appearance of new bright scatterers in a SAR image time series. An alternative approach to sail statistics considers sail spacings or sail-to-sail distances. A new sail cuts the spacing into two, and if the probability for this to happen does not depend on the spacing, the spacing distribution is asymptotically lognormal, as shown by (Kolmogorov, 1941). As the RSN and the number of spacings are about equal for ridge segments, the probability that a new ridge appearing in the profile ends in a certain segment is then proportional to the RSN of the segment. This indicates that the applicability of lognormal and hypergeometric models have the same physical origin. The lognormal has also been found to apply to sail spacings in the Baltic since (Lewis et al., 1993). Another hint of the background physical process is that the BPN statistics is parameterisable by pixel block side length L rather than area L^2. The length of ridge sails typically exceeds L, and thus a ridge formation event does not add bright scatterers pixelwise but as a chain crossing the pixel block.

In the high-resolution SAR, it was likely that most bright pixels indicate ridge rubble. Their statistics were studied using binary images, and no attempt was made to interpret the intensity variations of the bright pixels, although it may be noted that they followed exponential distribution. It was observed that the bright pixel texture in dense ridge fields was not much different from that of ship channels that are flat rubble beds. All studied BPP values generated more or less the same contextual images. This suggests that the correlation between sail height and SAR intensity is weak. It remains to be investigated whether connectedness, curvature and other measures may provide ridge height estimates.

High-resolution SAR data provide a kind of baseline for the investigations on ridge parameter retrieval as the returns have a connection both with ground truth ridging statistics and with the backscattering models by (Manninen, 1992) and (Carlström and Ulander, 1995). The hypergeometric model provides a scale connection tool that can be used to study how lower resolution pixel intensities relate to the pixel statistics in higher resolution matching pixel blocks. Our high- and medium-resolution images did not have the required spatiotemporal overlap, unfortunately. However, the medium-resolution image did not appear much different in binary BPP versions, which mostly consisted of disconnected pixels and generated contextual images that enhanced the ridging features in a similar way for a wide range of BPP values. Also, the simulation algorithm applied to the medium-resolution image as well as the Gamma distribution asymptotics of the hypergeometric model.

Relying on the results obtained in (Mäkynen and Hallikainen, 2004) for the scatterometer data at X- and C-band and (Dierking, 2010) for L-band SAR imagery, it can be hypothesised that the results for C-band and L-band would follow similar lines. A possible obstacle to the presented analysis occurs when the air temperature is warm enough to make the snow cover wet. As shown by (Mäkynen and Hallikainen, 2004), this essentially decreases the contrast between level and deformed ice, and thus it is uncertain whether the proposed method applies in the wet snow conditions. However, for this not to happen, any change in

ambient conditions should severely overturn the order of BPN values, otherwise the persistence of contextual category images demonstrated in Section 3.6 would prevail. In addition, higher ridges are often snow-free and less affected by wet conditions. Further studies applying matching multiplatform data with different resolutions and varying ambient conditions are needed to clarify this and other unanswered issues left open.

5   *Data availability.* The LIDAR data is available at PANGAEA under the following DOI: https://doi.pangaea.de/10.1594/PANGAEA.930545 (Haas et al., 2021).

Author contributions. ML has main responsibility on analysis and writing about the high resolution SAR data and MS about the medium resolution SAR data. The rest of the text is joint work.

Competing interests. The authors declare that they have no conflicts of interest.

10   *Acknowledgements.* This work was supported by the EU, Finland, Norway, the Russian Federation and Sweden through the Kolarctic Cross Border Collaboration Project 'Ice Operations' under Grant KO2100 ICEOP. We thank Alexandru Gegiuc for the rectification of the SAR images. We also are grateful to Dr Marko Mäkynen for helpful discussions.

References

Albert, M.D., Lee Y.U., Ewe, H., and Chuah, H.: Multilayer Model Formulation and Analysis of Radar Backscattering from Sea Ice, Prog. Electromagn. Res., 128, 267-290, https://doi.org:10.2528/PIER12020205, 2012.

Breiman, L.: Random forests, Machine Learning, 45, 5–32, 2001.

Calström, A., Ulander, L. M. H.: Validation of backscatter models for level and deformed sea ice in ERS-1 SAR images, Int. J. Remote Sens., 16, 3245–3266, 1995.

Carlström, A., Ulander, L.M.H.,and Dierking, W. Radar Scattering Models and ERS-1 SAR Data Inversion for Baltic Sea Ice. In Baltic experiment for ERS-1 (BEERS). Edited by L.M.H. Ulander. Winter Navigation Research Board, National Maritime Administration, Norrköping, Sweden. Research Report 51, pp. 35–70, 1994.

Calström, A., Ulander, L. M. H.: Validation of backscatter models for level and deformed sea ice in ERS-1 SAR images, Int. J. Remote Sens., 16, 3245–3266, 1995.

Carlstrom, A.: A microwave backscattering model for deformed first-year sea ice and comparisons with SAR data, IEEE T. Geosci. Remote S., 35, 378–391, https://doi.org/10.1109/36.563277, 1997.

Dierking, W. Multifrequency scatterometer measurements of Baltic Sea ice during EMAC-95, Int. J. Remote Sens., 20:2, 349–372, https://doi.org/10.1080/014311699213488, 1999.

(Dierking, W. Mapping of Different Sea Ice Regimes Using Images From Sentinel-1 and ALOS Synthetic Aperture Radar, IEEE T. Geosci. Remot S., 48(3):1045 1058 https://doi.org/10.1109/TGRS.2009.2031806, 2010)

Dumitru, C.O., Datcu, M.: Information content of very high resolution SAR images: Study of feature extraction and imaging parameters. IEEE T. Geosci. Remote S., 51, 4591–4610, https://doi.org/10.1109/TGRS.2013.2265413, 2013.

Eicken, H., Gradinger, R., Salganek, M., Shirasawa, K., Perovich, D.K., Leppäranta, M. (eds.): Sea ice field research techniques. University of Alaska Press, Fairbanks, Alaska, 2009.

Eriksson, L.E.B. et al. Evaluation of new spaceborne SAR sensors for sea-ice monitoring in the Baltic Sea, Can. J. Remote Sensing, 36, S56–S73, https://doi.org/10.5589/m10-020, 2010.

Fredensborg Hansen, R. M., Rinne, E., Farrell, S. L., Skourup, H.: Estimation of degree of sea ice ridging in the Bay of Bothnia based on geolocated photon heights from ICESat-2, The Cryosphere, 15:6, 2511-2529, https://doi.org/10.5194/tc-15-2511-2021, 2021.

Fritz, T., Eineder, M. (eds.): TerraSAR-X Basic Product Specification Document. TX-GS-DD-3302. Airbus DS 2013. Available online: **https://sss.terrasar-x.dlr.de/docs/TX-GS-DD-3302.pdf** (accessed on 19 May 2021).

Gegiuc, A., Similä, M., Karvonen, J., Lensu, M., Mäkynen, M., and Vainio, J.: Estimation of degree of sea ice ridging based on dual-polarized C-band SAR data, The Cryosphere, 12, 343-364, 2018.

Johansson, R. , Askne, J., Modelling of radar backscattering from low-salinity ice with ice ridges, Int. J. Remote Sens. 8, (11), 1667–1677, 1987.

Haas, C., Lobach, J., Hendricks, S., Rabenstein, L., and Pfaffling, A.: Helicopter-borne measurements of sea ice thickness, using a small and lightweight, digital EM system, J. Appl. Geophys., 67, 234–241, https://doi.org/10.1016/j.jappgeo.2008.05.005, 2009.

Haas, C., Casey, A., Lensu, M.: Safewin 2011 airborne EM sea ice thickness measurements in the Baltic Sea. PANGAEA, https://doi.pangaea.de/10.1594/PANGAEA.930545, 2021.

Hallikainen, M.: Microwave remote sensing of low-salinity sea ice. In F. Carsey (Ed.), Microwave Remote Sensing of Sea Ice, 361–373. Washington D.C.: AGU, 1992.

Karvonen, J., Simila, M., and Mäkynen, M.: Open water detection from Baltic Sea ice Radarsat-1 SAR imagery, IEEE Geosci. Remote S. Letters, 2, 275–279, https://doi.org/10.1109/LGRS.2005.847930, 2005.

Kolmogorov, A.N.: On the log-normal distribution of particles sizes during breakup process. Dokl. Akad. Nauk. SSSR, 99–101, 1941.

Kuuliala, L., Kujala, P., Suominen, M., and Montewka, J.: Estimating operability of ships in ridged ice fields, Cold Regions Science and Technology, 135, 51–61, https://doi.org/10.1016/j.coldregions.2016.12.003, 2016.

Lensu, M.: The evolution of ridged ice fields. Helsinki University of Technology, Ship Laboratory report series M, 280, 140, 2003.

Leppäranta, M., Hakala, R.: The structure and strength of first-year ice ridges in the Baltic Sea, Cold. Reg. Sci. Technol., 20:3, 295–311, https://doi.org/10.1016/0165-232X(92)90036-T., 1992.

Lewis, J. E., Leppäranta, Granberg, H. B.: Statistical properties of sea ice surface topography in the Baltic Sea. Tellus, 45 A, 127–142, https://doi.org/10.3402/tellusa.v45i2.14865, 1993.

Manninen, A. T.: Effects of ridge properties on calculated surface backscattering in BEPERS-88. Int. J. Remote Sens, 13, 2469–2487, https://doi.org/10.1080/01431169208904282, 1992.

Manninen, A. T.: Surface morphology and backscattering of ice-ridge sails in the Baltic Sea. Journal of Glaciology, 42, 141–156, 1996.

Melling, H.: Detection of features in first-year pack ice by synthetic aperture radar (SAR), Int. J. Remote Sens., 19:6, 1223–1249, https://doi.org/10.1080/014311698215702, 1998.

Mock, S. J., Hartwell, A. D., Hibler III, W. D.: Spatial aspects of pressure ridge statistics, J. Geophys. Res. 77 (30), 5945–5953, https://doi.org/10.1029/JC077i030p05945, 1972.

Mäkynen, M., Manninen, A., Similä, M., Karvonen, J., Hallikainen, M.: Incidence Angle dependence of the statistical properties of the C-Band HH-polarization backscattering signatures of the Baltic sea ice, IEEE T. Geosci. Remote S., 40, 2593–2605, 2002.

Mäkynen, M., Hallikainen, M.: Investigation of C- and X-band backscattering signatures of the Baltic Sea ice., Int. J. Remote Sens., 25, 2061–2086, 2004.

Palosuo, E., Leppränta, M., Seinä, A.: Formation, thickness and stability of fast ice along the Finnish coast, Styrelsen för vintersjöfarts-forskning. Research report. No.36. Finland. 19p. + appends. 1982.

Ronkainen, I., Lehtiranta, J., Lensu M., Rinne, E., Haapala, J., Haas, C.: Interannual sea ice thickness variability in the Bay of Bothnia, The Cryosphere, 12:11, 3459–3476, https://doi.org/10.5194/tc-12-3459-2018, 2018.

Similä, M., Leppäranta, M., Granberg, H. B, Lewis, J. E.: The relation between SAR imagery and regional sea ice ridging characteristics from BEPERS-88, Int. J. of Remote Sens., 13:13, 2415–2432, https://doi.org/10.1080/01431169208904279, 1992.

Similä, M, Arjas, E., Mäkynen, M., and Hallikainen, M.: A Bayesian classification model for sea ice roughness from scatterometer data, IEEE T. Geosci. Remote S., 39, 1586–1595, https://doi.org/10.1109/36.934090, 2001.

Similä, M., Mäkynen, M, Heiler, I.: Comparison between C band synthetic aperture radar and 3D laser scanner statistics for the Baltic Sea ice, J. Geophys. Res.- Oceans, 115, C10 https://doi.org/10.1029/2009JC005970, 2010.

Similä, M. and Lensu, M.: Estimating the Speed of Ice-Going Ships by Integrating SAR Imagery and Ship Data from an Automatic Identification System. Remote Sens. 10, 1132. https://doi.org/10.3390/rs10071132, 2018.

WMO Sea ice Nomenclature, WMO n. 259 (rev, 2010), 2010.